

Infrared observations of serendipitous hard *Chandra* X-ray sources

C.S. Crawford, A.C. Fabian, P. Gandhi, R.J. Wilman and R.M. Johnstone

Institute of Astronomy, Madingley Road, Cambridge CB3 0HA

31 October 2018

ABSTRACT

We present observations of a sample of optically-faint, hard X-ray sources of the kind likely to be responsible for much of the hard X-ray background. We confirm that such sources are easily detected in the near-infrared, and find that they have a featureless continuum suggesting that the active nucleus is heavily obscured. The infrared colours of the majority of the targets observed are consistent with absorbed elliptical host galaxies at $z = 1 - 2$. It is likely that we are observing some of the brighter members of the important new class of X-ray Type II quasars.

Key words:

diffuse radiation – X-rays: galaxies – infrared: galaxies – galaxies: active

1 INTRODUCTION

The X-ray Background (XRB) above 2 keV has at last been mostly resolved into point sources by the *Chandra* X-ray Observatory (Mushotzky et al 2000; Brandt et al 2000). *Chandra*'s superb sub-arcsecond imaging provided the high-sensitivity confusion-less images for this breakthrough.

The generally accepted model for the XRB is that it is dominated by absorbed active galactic nuclei (AGN; Setti & Woltjer 1989; Madau, Ghisellini & Fabian 1994; Comastri et al 1995), a significant fraction of which are Compton-thick (i.e. have an absorbing column $> 10^{24} \text{ cm}^{-2}$): collectively such objects are Type II AGN. So far, only the 2-7 keV XRB has been (mostly) resolved with *Chandra*. This regime is not expected to be sensitive to large numbers of Compton-thick objects, where the X-ray emission emerges only above 5 keV (Wilman & Fabian 1999; Wilman, Fabian & Nulsen 2000); it should reveal sources with column densities more typically of $10^{22-23} \text{ cm}^{-2}$. The Compton-thick objects provide much of the power where the XRB spectrum peaks in νI_ν . Correction of the XRB for absorption (Fabian & Iwasawa 1999) shows that accretion at the standard 10 per cent efficiency onto massive black holes can approximately account for the local mass density in black holes (Magorrian et al 1998) and that about 85 per cent of that accretion power is absorbed and re-radiated in the mid-to far-IR.

Despite the recent progress resolving the hard XRB into discrete sources with the correct collective spectrum, the actual identification of many of these objects is, however, not straightforward. Roughly one-third are blue broad-line quasars, another third are identified with faint, optically-normal galaxies and the final third have only extremely faint optical counterparts or no detectable counterpart at all (Mushotzky et al 2000; Brandt et al 2000; Maiolino et al 2000). Mushotzky et al (2000) find infrared HK' band counterparts for most of their X-ray detected sources.

We have used SCUBA maps of the cores of the lensing clusters

A2390 and A1835 to place deep submillimetre limits on the three serendipitous *Chandra* sources which lie in the field (Fabian et al 2000). Only one (marginal) source is detected in both the X-ray and submillimetre bands. Of three X-ray sources in the HST field of A2390 we find that one plausibly has a photometric redshift of 0.9 and conclude from its hard X-ray spectrum that it is a Type II quasar; the other two have $V > 26$ (Fabian et al 2000). Such objects are therefore difficult to follow up in the optical band alone. Although two SCUBA sources in the A370 field that optically resemble AGN are detected in X-rays (Bautz et al, in preparation), none of the 10 SCUBA sources in fields flanking the Hubble Deep Field is detected in a deep *Chandra* observation (Hornschemeier et al 2000).

In this paper we present observations which are part of a programme to determine the origin of the optically-faint, hard X-ray sources that are most likely responsible for the hard X-ray background. Given the possibility that the sources are highly redshifted and/or obscured, we have sought infrared counterparts at the X-ray target position. Our work bridges other surveys in this field which are either very deep, or shallow with a wider area coverage. By targeting the serendipitous sources from several 10-20 ksec *Chandra* observations, we are able to select the very brightest absorbed sources in each field for follow-up.

2 SELECTION AND PROPERTIES OF X-RAY TARGETS

The X-ray sources were selected from those found serendipitously in the field of *Chandra* observations of galaxy clusters obtained during the Guaranteed Time of one of us (ACF). These observations were typically of 10-20 ksec duration (see Table 1) and all were taken so that the on-axis pointing position fell on the ACIS-S3 detector, apart from that with sequence number 800010. We shall present a detailed analysis of the X-ray properties of the entire sample of serendipitous sources elsewhere; here we detail follow-up

arXiv:astro-ph/0005242v1 11 May 2000

observations of a preliminary small sample of sources of a very specific type.

We examined each of the cluster fields for serendipitous sources using the Chandra Interactive Analysis of Observations (CIAO) detection software. All three available detect algorithms (celldetect, wavdetect and vtpdetect) were used in order to search for sources under the different assumptions and methods that each employ. In the first instance, we ran the detect software on unbinned data in three energy bands: 0.5-7 keV, ‘soft’ 0.5-2 keV and ‘hard’ 2-7 keV. Those sources with detectable hard counts were then selected for more detailed follow-up. As detailed later (section 4.5), the higher sensitivity of *Chandra* below 2 keV means that even genuinely hard sources can still show plenty of counts in our soft band. Most of the sources in this paper were detected close to the pointing position, either in the S3 or S2 chips. The exceptions were the two sources in the field of A2199 (CXOU J162850.9+392434 and CXOU J162827.8+392343), which were both in I3, and CXOU J031946.4+413734 and CXOU J031946.2+413737 in the Perseus field which were in the I2 chip. The sources were 2-9 arcminutes off-axis, with a reduced effective area down to 80 per cent of the on-axis value.

We calculated the number of counts in each of these three energy bands using a box typically of side 16 pixels (8 arcsec; although the box size was increased for sources well off-axis, ie for CXOU J162827.8+392343, CXOU J091340.9+410314 and CXOU J140048.4+024954) from which to extract the source counts. The background countrate was estimated from a box around the source (excluding the source box) of sidelength typically 55 pixels (27.5 arcsec; or larger for those objects with countrate extracted from a larger source box). The only exception was in the case of CXOU J031946.4+413734 and CXOU J031946.2+413737 in the Perseus field, where the sources were so close that the background rate for both was estimated from a close region of sky. The counts in all three energy bands, as well as the ratio of soft/hard counts are given in Table 1.

As the *Chandra* observations were relatively early on in the operation of the satellite, all were affected by inaccuracies in the aspect solution during the initial pipeline processing of the data. This led to offsets of up to 8 arcseconds between the coordinate positions given by *Chandra* and those of the sky. This offset was easy to correct for in the observations of IRAS 09104+4109 (800017) and Perseus (800010), where the position of the AGN can be determined with half-arcsecond precision from the *Chandra* hard-band image, to be compared to sub-arcsecond radio core position. A hard nuclear peak was not, however, found in the *Chandra* images of A1795, A1835 or A2199, so the X-ray optical registration was done by a systematic cross-correlation between *all* the X-ray sources against optical sources from the Digitized Sky Survey (DSS). Through this process we improved the accuracy of the attitude solution to within about 2 arcseconds. Note we assume that only a simple translation in sky coordinates is required, with no rotation or stretching. The (registered) X-ray source positions were then compared to optical sources on the DSS. Although we have been using multi-colour (archival) optical imaging data of our fields, many of the sources lie a few arcmin out from the centre of the cluster, and are not always covered by previous observations.

This inaccurate aspect solution to the X-ray data and the uncertainties inherent in the correction of the *Chandra* coordinates to the sky presents some confusion when applied to conventional naming of the source. The coordinates used to name the source are derived from a definite ID of the source from IR imaging presented later in this paper. Where no source is detected in the IR imaging

we use the IR-detected sources within this field to apply the correct offset between the *Chandra* frame of reference and the sky, and thus derive the source name.

We selected our targets from those sources that had a soft-to-hard (S/H) ratio of less than 3.5 (see Table 1; also section 4.5 for implications of the S/H ratio), and either a very faint, or no, optical identification on the DSS. The exceptions were two intriguing sources in the ACIS-I observation of the Perseus cluster. Their unusually close proximity to each other (5 arcsec) and exact association with two close optical sources marked them out as particularly interesting and worthy of detailed follow-up. The DSS B- and R-band images around each source observed in this paper are shown in Fig 1, along with matching *Chandra* images in the 0.5-7 keV, 0.5-2 keV and 2-7 keV energy bands. Faint optical identifications are visible not only for CXOU J031946.4+413734 and CXOU J031946.2+413737, but also CXOU J091357.5+405938, CXOU J162827.8+392343 and (perhaps) CXOU J091360.0+405548. The faint optical source seen in the CXOU J134905.8+263752 box is several arcseconds away from the X-ray position, and thus we assume it is not associated.

3 OBSERVATIONS

3.1 Optical spectra

Optical spectra of the close X-ray sources CXOU J031946.4+413734 and CXOU J031946.2+413737 were obtained in service time with the ISIS double beam spectrograph on the William Herschel Telescope (WHT) on La Palma, during the night of 1999 Dec 15. The 1 arcsec-wide slit was oriented at a position angle of 138° in order to detect the emission from both sources. The total exposure was 3000 s, and the R158R and R158B gratings were used to produce a wavelength range of 3500-5500Å on the EEV chip in the blue arm, and 5150-8050Å on the Tek chip in the red arm of the instrument. The data were bias-subtracted, flat-fielded, wavelength-calibrated from exposures of an arclamp, and corrected for the Galactic extinction of $E(B-V)=0.31$ in this direction.

3.2 Infrared observations

Near-infrared spectra and images were taken during the nights of 2000 Feb 24-25 at the United Kingdom Infrared Telescope (UKIRT) in Hawaii. The night of Feb 24 was of very good seeing and transparency, both of which, however, deteriorated by the time of our observations on Feb 25. We used two instruments: the 2D grating spectrometer CGS4, and the cooled infrared camera IR-CAM3/TUFTI. A full log of observations is shown in Table 2.

CGS4 was used with the 40 l/mm grating on the long camera, yielding a pixel scale of 0.618 arcsec per pixel. The slit width was set to 4 pixels (ie 2.47 arcsec), and observations were taken using the standard ‘quad-slide’ nodding pattern of a-b-b-a along the slit. Spectra were taken in the first order in each of the H and K bands on some objects, as well as of corresponding spectrophotometric and atmospheric absorption standards in the same band. The data were reduced using the standard reduction package CGS4DR V1.3-0. The object spectrum was divided by the spectrum of a standard star observed at approximately the air mass, assumed to approximate to a black body, in order to remove any common atmospheric features. The object spectra were flux-calibrated using a standard star; the flux calibration was estimated to be accurate to within ten

per cent. The final, calibrated spectrum of the object was extracted from three rows centred on the object peakup row, and three rows around the sky peakup row 19 pixels away.

IRCAM3/TUFTI is an imaging camera with a scale of 0.0814 arcsec/pixel, and a total field of view of 20.8×20.8 arcsec. TUFTI was used in ND STARE mode, with standard read-out. Objects were observed using a jitter grid of 9 points, each separated by 6 arcsec. We observed for 60 s at each of the grid points, except for CXOU J140100.2+025720, leading to total exposure time of 540 s in each of the J, H and K bands. The imaging observations for CXOU J140100.2+025720 were curtailed because we were approaching the end of that night's observing. The data were reduced using the standard ORACDR reduction package available from UKIRT, and flux-calibrated using observations of several standard stars in the same bands.

4 RESULTS AND DISCUSSION

4.1 X-ray luminosities

We derive the bolometric luminosity of the X-ray sources from the observed 0.5-7 keV count rate, assuming the emission originates in a non-thermal power-law with photon index of $\Gamma = 2$, subject only to Galactic absorption. The observed 0.5-7 keV fluxes range over $4.3 - 63.3 \times 10^{-15}$ erg cm $^{-2}$ s $^{-1}$ (Table 1), implying a bolometric luminosity range of $1.7 - 24.8 \times 10^{44}$ and $9.0 - 130.8 \times 10^{45}$ erg s $^{-1}$ for redshifts of 0.5 and 3 respectively.

4.2 Optical spectra

The optical spectra of CXOU J031946.4+413734 and CXOU J031946.2+413737 are shown in Fig 2. CXOU J031946.4+413734 (the optically-fainter, X-ray-harder source to the south-east) has a solitary broad line observed at 6454Å, with a FWHM of 5460 km s $^{-1}$ and an intensity of 1.6×10^{-15} erg cm $^{-2}$ s $^{-1}$. The most likely identification for this is MgII, implying a redshift for the source of $z = 1.307$; however we do not obviously see CII] λ 2336 or CIII] λ 1909 emission line at 5365Å and 4404Å, or H α at 1.514 μ m in the infrared spectrum (Fig 3; the 2- σ emission line nearby is at 1.504 μ m). The line can only be CIII] if the expected Ly α at 4110Å is completely extinguished by dust absorption; it is unlikely to be Ly α itself, as the continuum does not cut off due to a Ly α -forest as expected for a source at $z = 4.3$. CXOU J031946.2+413737 shows a relatively featureless continuum, with too little flux for a reliable redshift to be obtained from cross-correlation with a template galaxy spectrum.

4.3 Infrared spectra

We detected continuum emission from four of the objects observed with CGS4, only failing to detect any signal at the position of CXOU J091360.0+405548 at an upper limit of 5.1×10^{-19} erg s $^{-1}$ cm $^{-2}$ Å $^{-1}$. (CXOU J091360.0+405548 is the source we also failed to detect from the infrared imaging, see next section). All the detected objects have flat infrared spectra with no significant emission-line features (Fig 3). Where magnitudes from the infrared imaging are available (see next section), they are compatible with the spectra (see Fig 3 for a direct comparison). The flux inferred from the infrared imaging tends to be higher than that determined from the spectra, which is to be expected if our slit placement does not quite cover all the light from the object.

We searched for emission lines in those parts of the infrared spectrum least affected by any OH atmospheric absorption (if the sky is variable then we may not be able to correct for these features fully in the data reduction and spurious emission lines would be introduced; these regions of the spectrum are shown by the dotted lines in Fig 3). We find no significant emission lines, with 3- σ upper limits to the equivalent width of 185-720Å in H, and 145-190Å in K (depending on the length of the exposure). We would expect some Balmer or Paschen line emission to be visible for targets in most of the redshift range $0 < z < 4$, and MgII to be visible for sources $4.3 < z < 5.4$. It is thus surprising that none of our targets show strong emission lines in the CGS4 spectra. This suggests that any active nucleus – and any ionized gas that surrounds it – is heavily obscured.

4.4 Infrared imaging

Of the nine sources imaged in good seeing conditions, we detect infrared sources in the 21×21 arcsec TUFTI field of view for eight of them. A further three objects attempted during conditions of poor seeing and transparency were not detected. Due to the variability of the conditions we are unable to quantify the detection limits. CXOU J091360.0+405548 (our least significant X-ray source) was not detected to a 3- σ limit of 22.66 in J, 22.27 in H and 21.62 in K (assuming a point source). The J, H and K-band TUFTI images are shown in Fig 4 for all sources where infrared sources were found in the field. In Table 3 we list the infrared magnitudes (and estimated DSS B and R magnitudes or limits) of each source near the centre of the TUFTI image, along with its offset from the boresight of TUFTI (and thus from the X-ray position). The position of this aim-point and its constancy was established from the observations of standard stars throughout the night.

There is a very clear single identification of a source near the centre of the TUFTI field of view for seven of the eight sources shown in Fig 4. The source for CXOU J140106.9+024934 is resolved into three separate components in the K band. CXOU J091352.8+405829 is the only source (out of those closest to the centre) to show any significant ellipticity. The registration of the X-ray coordinates to the sky (as indicated by the offset of the source from the aimpoint of TUFTI) is, not surprisingly, best in the field of IRAS 09104+4109, the source with a clear detection of the point-like AGN at hard energies to cross-correlate with the radio position. Offsets are larger for the other fields, but all are good to within 2.1 arcsec. Only CXOU J140100.2+025720 has no clear identification, as there are two sources that are both at a larger offset from the centre than expected: it is not clear that either of these are the identification of the X-ray source. For clarity we will, however, refer to them as CXOU J140100.2+025720 (SSE) and (ESE), according to the direction of the offset from the position of the X-ray source CXOU J140100.2+025720. There is no correlation between the J-K colours of our detected objects and the ratio of their soft to hard X-ray flux, but this is not unexpected as we have deliberately chosen a very small range of X-ray flux ratio to investigate in the first place.

4.5 Absorbed AGN?

We consider it unlikely that our detected objects are optically-faint stars, as any star with a sufficient level of X-ray activity is unlikely to show such a featureless infrared continuum. The infrared colours of our detected targets are very different to those of main sequence,

giant and supergiant stars of all spectral types (Fig 5), although the infrared colours alone are consistent with some IR-selected stars (eg the samples shown in Fig 5 of Dickinson et al 2000). We note also that stars comprised only 6 per cent of the sources found in the ROSAT Deep Survey (Schmidt et al 1998). The infrared colours of our sources are better matched to those of X-ray-selected quasars in the compilation of Elvis et al (1994).

We performed a simple X-ray spectral analysis of the two brightest sources, CXOU J134905.8+263752 and CXOU J134849.0+263716 using XSPEC. The spectra were fitted with power-law models of fixed photon index $\Gamma = 2$, absorbed (in our frame) by a column density N_{H} . The X-ray spectra require excess column densities of $N_{\text{H}} = 2.6 \pm 0.7$ and $3.5_{-1.1}^{+1.3} \times 10^{21} \text{ cm}^{-2}$, for CXOU J134905.8+263752 and CXOU J134849.0+263716 (errors are $1\text{-}\sigma$). For example, the fit to CXOU J134905.8+263752 for a power-law model (of fixed $\Gamma=2$) with only the Galactic absorption gives $\chi^2=24.5$ (for 12 degrees of freedom), improving to $\chi^2=6.1$ (for 11 d.o.f.) when the absorption is allowed to vary freely, giving $N_{\text{H}} = 2.6 \pm 0.7 \times 10^{21} \text{ cm}^{-2}$ (Fig 6). A fit with the absorption fixed at Galactic, and now with the power-law slope varying freely yields $\Gamma = 1.4 \pm 0.14$, with $\chi^2=9.6$ (11 d.o.f.), and a completely free fit gives $\Gamma = 1.9 \pm 0.2$ and $N_{\text{H}} = 2.3 \pm 0.9 \times 10^{21} \text{ cm}^{-2}$, with $\chi^2=6.06$ (for 10 d.o.f.). Thus there is a greater than 95 per cent probability that the source requires excess absorption over the Galactic column. The models with $\Gamma = 2$ and free N_{H} predict de-absorbed fluxes at 1keV of $2.0 \pm 0.3 \times 10^{-5}$ and $8.8_{-1.7}^{+1.8} \times 10^{-6}$ photons $\text{cm}^{-2} \text{ keV}^{-1} \text{ s}^{-1}$ for CXOU J134905.8+263752 and CXOU J134849.0+263716 respectively (equivalent to 13 and 6 nJy).

We converted these de-absorbed fluxes at 1keV to intrinsic K-band magnitudes, assuming a spectral index of $\alpha_{\text{KX}} = 1.16$ (such that $S \propto \nu^{-\alpha}$). This index is the median for the sample of 41 quasars in Elvis et al (1994), who chose optically-bright objects with high signal-to-noise ratio *Einstein* X-ray spectra. They are predominantly low redshift objects, so K-corrections should be negligible. The predicted K-band magnitude of 17.3 for CXOU J134905.8+263752 is slightly fainter than the observed value of 17.01 ± 0.06 , whereas the predicted magnitude of 18.2 for CXOU J134849.0+263716 is a lot brighter than the observed value of 19.99 ± 0.25 . This suggests that for the total K-band light of CXOU J134849.0+263716 to be due wholly to the AGN continuum, it must be reddened by ~ 2 magnitudes at K. For a Galactic dust-to-gas ratio, this equates to $N_{\text{H}} = 3.5 \times 10^{22} \text{ cm}^{-2}$, substantially more than the value derived from the X-ray fitting.

We extend this calculation to predict optical and infrared magnitudes for all our TUFTI-detected sources, assuming that all the emission is due to a typical quasar at a range of redshifts. We use PIMMS to obtain the normalization of the quasar spectral energy distribution (SED) at 1 keV from the observed 0.5-7 keV count rate, assuming $\Gamma = 2$ using the Galactic column. We then extrapolate from the inferred X-ray flux at 2 keV using the (rest-frame) SED of a typical radio-quiet quasar, approximated from that given in Elvis et al (1994); $\alpha_{\text{OX}} = 1.4$ (bridging the monochromatic luminosities at 2500Å and 2keV), $\alpha = 0.15$ (over 0.25-1.28 μm), $\alpha = 2.38$ (1.28-1.85 μm) and $\alpha = 1.38$ ($>1.85\mu\text{m}$).

For all the sources, the observed SEDs are redder in slope than that expected from the quasar predictions (Fig 7). The majority of the objects have unabsorbed quasar predictions that are insufficient (by up to 1.5 magnitudes) to account for the observed magnitudes, suggesting that the AGN continuum is not the main contributor to the infrared magnitudes. Where the (low-redshift) quasar SEDs are more compatible with the observed infrared magnitudes (CXOU

J091340.9+410314, CXOU J134905.8+263752) the quasar SED still overestimates the optical band limits. There remains only one source (CXOU J134849.0+263716) where the extrapolated spectrum vastly overestimates the observed magnitudes; here any AGN component must be reddened by at least 1.5 magnitudes in the infrared. These results are, however, sensitive to the α_{OX} used: varying α_{OX} by only ± 0.1 leads to a corresponding ± 0.6 mag variation in the optical-infrared magnitudes shown in Fig 7. Even if α_{OX} is adjusted so that the quasar can account for all of the K-band light, its continuum must be highly reddened to also fit the observed B and R limits or magnitudes (we assume that the lack of detection in the optical is not due to variability). The results indicate both that a host galaxy contributes much of the infrared light of many of our sources, and that any contribution from the quasar continuum requires significant reddening.

Further constraints on the redshift and N_{H} may be obtained by comparing the soft to hard (S/H) count ratios (Table 1) with those predicted by XSPEC models, as shown in Table 4 and Fig 8. For a given model (ie z and N_{H}), the differences between the predictions for the two brightest sources reflect the different response matrices of the front- (CXOU J134905.8+263752 on S2) and back- (CXOU J134849.0+263716 on S3) illuminated CCDs. The observed S/H ratios are 2.4 ± 0.4 (for CXOU J134905.8+263752) and 2.5 ± 0.5 (for CXOU J134849.0+263716). Very roughly, the values in Table 4 suggest that if our two sources had power-law spectra, they have $N_{\text{H}} \sim 10^{22} \text{ cm}^{-2}$ if at low redshift, or more like $N_{\text{H}} \sim 10^{23} \text{ cm}^{-2}$ if at $z \geq 1$. As a first approximation, the Tables may also be used to interpret the S/H count ratios for the other sources, for which there are insufficient counts to justify spectral fitting [using the CXOU J134905.8+263752 (and CXOU J134849.0+263716) predicted values as guides for sources on the front- (back-)illuminated chips]. We have attempted simple spectral fitting of the sources with around 50 counts, and although the error bars are larger, the results confirm the conclusions of Table 4. The X-ray colours of all our sources are consistent with the X-ray emission originating in an AGN at a range of redshift, but *only* if that emission is absorbed by an intrinsic column density of at least $N_{\text{H}} \sim 10^{22} \text{ cm}^{-2}$ at $z > 0.5$. We conclude that the bulk of our objects have X-ray column densities which classify them as Compton-thin Type II objects.

4.6 Photometric redshifts

Given that at least one of the detected infrared objects is resolved to have significant ellipticity, and that the host galaxies of AGN usually make the dominant contribution to the near-infrared light of AGN (Rix et al 1999), we also compare the infrared colours and magnitudes to those of galaxies at a range of redshift. The lack of strong emission lines in the infrared spectra argues against strong starburst behaviour, so we consider only elliptical galaxies. We used the programme HYPERZ (Bolzonella, Pello & Miralles 2000), which fits a grid of template galaxy spectra (generated from the GISEL library; Bruzual & Charlot 1993) to the observed magnitudes, with variations permitted in the age, redshift and intrinsic reddening. We attempted a variety of fits: a 3 Gyr-old elliptical galaxy (with e-folding time τ of 1 Gyr) fitted without and with the possibility of intrinsic reddening; and a choice between an elliptical galaxy at ages 1.5, 3 and 5 Gyr again without and then with reddening. In all cases we assumed the reddening law of Calzetti et al (2000) and constrained the age so that it did not exceed the age of the Universe at the redshift under consideration (assuming $H_0 = 50 \text{ km s}^{-1} \text{ Mpc}^{-1}$). The maximum redshift considered was $z = 6$.

Our results for the basic model (a 3 Gyr-old elliptical with no intrinsic reddening) are shown for three of our detected sources in Table 5. We also plot the best-fit solutions for this model to CXOU J134905.8+263752, CXOU J134849.0+263716 and CXOU J140106.9+024934 in Fig 9. Increasing the range of possible elliptical galaxy ages, and/or allowing the possibility of intrinsic reddening to this model decreased the χ^2 , but broadened the range of possible redshifts, and sometimes introduced a secondary χ^2 minimum at lower redshift. Without deeper optical limits it is hard to constrain the redshift in any detail; we can only say that the infrared colours are not inconsistent with an origin from elliptical galaxies above a redshift of one.

Host galaxies to radio-quiet quasars generally have a modest luminosity of just less than, or around that of an L^* galaxy, with radio-loud quasars lying in galaxies a factor of 2-5 times brighter (Rix et al 1999). We thus also compare our observed infrared magnitudes to those expected from a passively-evolving, unabsorbed L^* elliptical galaxy (R. McMahon & A. Aragon-Salamanca, private communication) in Fig 10. This crude comparison of magnitudes suggests that CXOU J140106.9+024934, CXOU J134849.0+263716 and CXOU J140100.2+025720 (ESE) are consistent with L^* galaxies at a redshift of $z = 2$, with other sources such as CXOU J140100.2+025720 (SSE), CXOU J091340.9+410314, CXOU J091352.8+405829 and CXOU J162827.8+392343 being nearer $z = 1$. The inferred redshifts may be underestimated, however, if the infrared colours and magnitudes also include a contribution from a central quasar continuum.

5 SUMMARY AND CONCLUSIONS

We have carried out follow-up observations of optically-faint, X-ray hard, serendipitous *Chandra* sources, and find that they are readily detected in the near-infrared. Spectra in the infrared of some of them appear flat and featureless, suggesting that strong emission-line activity is either absent or heavily obscured. Only one source – which is the brightest optically – shows a strong emission line in an optical spectrum, which we cannot identify unambiguously. The 0.5-7 keV fluxes of our sources are in the range $0.3 - 4.6 \times 10^{-14} \text{ erg cm}^{-2} \text{ s}^{-1}$ which, if due to an unabsorbed

non-thermal quasar spectrum, imply bolometric luminosities of a few times $10^{44} - 10^{46} \text{ erg s}^{-1}$, for redshifts between $0.1 < z < 3$. The X-ray colours of all our sources are consistent with an origin in quasars only if absorbed by an intrinsic column density of at least 10^{22} cm^{-2} . If we extrapolate a typical radio-quiet quasar spectrum at $0 < z < 3$ from the observed X-ray flux into the optical and infrared wavebands, we find that a host galaxy probably contributes much of the infrared light, and that the optical quasar continuum requires significant reddening. The infrared magnitudes and colours are consistent with a (host) $L \sim L^*$ galaxy at moderate redshifts $0.5 < z < 2.5$.

Although we do not have deep optical images for most of our objects, the limits imply that the optical and infrared properties may resemble so-called extremely red objects (EROs: see Scodreggio & Silva 2000 and references therein). These have proven difficult to follow up even with large telescopes, and good spectra and redshifts are only available for a small fraction. Whether there is a deeper, physical connection between optically faint Chandra sources and EROs must await larger samples of Chandra sources with deep optical and infrared coverage.

The properties of our small sample of objects is consistent with the existence of a population of moderately absorbed (i.e. Compton thin Type II) quasars at $z = 1 - 2$, as predicted by recent models for the hard XRB (Madau et al 1994; Celotti et al 1995; Comastri et al 1995; Wilman & Fabian 1999).

Finally, we note that the objects we have likely found, namely Type II quasars, are qualitatively different from Type II Seyferts. They do not obviously have any strong narrow-line region (although deeper spectra covering a wider band on more objects are needed to be definite on this issue), nor any obvious scattered blue continuum or blue light from star formation. They would not even be classified as active galaxies on the basis of what we have seen so far of their optical and infrared properties. It is only on the basis of the X-ray emission that we classify them as Type II objects, where Type II means strongly obscured (see also the discussion in Matt et al 2000). An appropriate name is X-ray Type II quasar. Of course, if 85 per cent of accretion power is absorbed (Fabian & Iwasawa 1999) then the objects dominating that power cannot have the broad torus opening-angles commonly ascribed to Seyfert galaxies. The simple and successful geometrical unification scheme for Seyfert galaxies (e.g. Antonucci 1993) cannot extend to quasars.

6 ACKNOWLEDGEMENTS

We are grateful to the *Chandra* project for the X-ray data, and to M. Bolzonella, R. Pello and J.-M. Miralles for making HYPERZ available. CSC and ACF thank the Royal Society, PG thanks the Isaac Newton Trust and the Overseas Research Trust, and RJW and RMJ thank the PPARC for financial support. We thank the service queue scheme on the William Herschel Telescope, which is operated on the island of La Palma by the Isaac Newton Group in the Spanish Observatorio del Roque de los Muchachos of the Instituto de Astrofísica de Canarias. The United Kingdom Infrared Telescope is operated by the Joint Astronomy Centre on behalf of the U.K. Particle Physics and Astronomy Research Council. This research has made use of the NASA/IPAC Extragalactic Database (NED), and the Digitized Sky Surveys which were produced at the Space Telescope Science Institute under U.S. Government grant NAG W-2166.

Please see separate figure

Please see separate figure

Figure 1. Blue and red DSS images (40 arcsec on a side) of the serendipitous *Chandra* sources. Next (from left to right) are presented the 0.5-7 keV, the soft (0.5-2 keV) and hard (2-7 keV) band *Chandra* images on the same scale. Where a box is drawn on an optical image it marks for comparison the central 13×13 arcmin of the TUFTI field shown in Fig 4.

REFERENCES

- Antonucci R., 1993, ARAA, 31, 473
 Bolzonella M., Pello R., Miralles J.-M., 2000, A&A, submitted (astro-ph/0003380)
 Brandt W.N. et al 2000, AJ, in press, (astro-ph/0002121)
 Bruzual G.A., Charlot S., 1993, ApJ, 405, 538
 Calzetti D., Armus L., Bohlin R.C., Kinney A.L., Koornneef J., Storchi-Bergmann T., 2000, ApJ, accepted for publication (astro-ph/9911459)
 Celotti A., Fabian A.C., Ghisellini G., Madau P., 1995, MNRAS, 277, 1169
 Comastri A., Setti G., Zamorani G., Hasinger G., 1995, A&A, 296, 1
 Dickinson M. et al 2000, ApJ, 531, 624
 Elvis M., Wilkes B.J., McDowell J.C., Green R.F., Bechtold J., Willner S.P., Oey M.S., Polowski E., Cutri R., 1994, ApJS, 95, 1
 Fabian A.C. et al 2000, accepted for publication in MNRAS, (astro-ph/0002322)
 Fabian A.C. & Iwasawa K.I., 1999, MNRAS, 303, L34
 Hornschemeier A.E. et al 2000, ApJ submitted, (astro-ph/0004260)
 Madau P., Ghisellini G., Fabian A.C., 1994, MNRAS, 270, L17
 Magorrian J. et al 1998, AJ, 115, 2285
 Maiolino R. et al 2000, A&A, 355, L47
 Matt G., Fabian A.C., Guainazzi M., Iwasawa K., Bassani L., Malaguti G., 2000, MNRAS submitted
 Mushotzky R.F., Cowie L.L., Barger A. Arnaud K.A., 2000, Nature, 404, 459
 Rix H.-W., Falco E., Impey C., Kochanek C., Lehar J., McLeod B., Munoz J., Peng C., 1999, to appear in *Gravitational Lensing: Recent Progress and Future Goals*, eds. Brainerd T., Kochanek C. (astro-ph/9910190).
 Stark A.A., Gammie C.F., Wilson R.W., Bally J., Linke R.A., Heiles C., Hurwitz M., 1992, ApJS, 79, 77
 Setti G., Woltjer L., 1989, A&A, 224, L21
 Schmidt M. et al, 1998, A&A, 329, 495
 Scodreggio M., Silva, D.R., 2000, A&A, submitted (astro-ph/0004228)
 Wilman R.J., Fabian A.C., 1999, MNRAS, 309, 862
 Wilman R.J., Fabian A.C., Nulsen P.E.J., 2000, submitted to MNRAS.

Figure 4. Infra-red images of the central 13×13 arcsec TUFTI field of view of the *Chandra* sources. North is to the top, and the small cross marks the position of the TUFTI boresight.

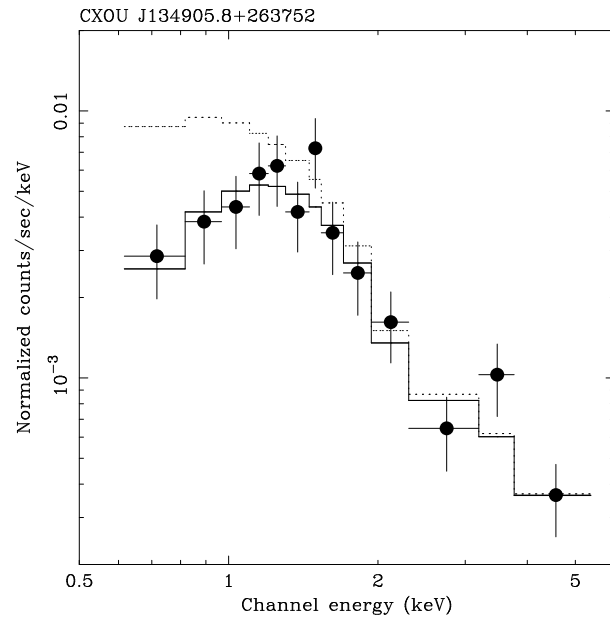


Figure 6. The X-ray spectrum of CXOU J134905.8+263752 (solid circle markers) together with best fitting $\Gamma = 2$ power-law model with free absorption (solid line). The effect of that model of changing the absorption to the Galactic value is indicated by the dotted line. The x-errors show the nominal bin width, whereas the y-errors are $1-\sigma$.

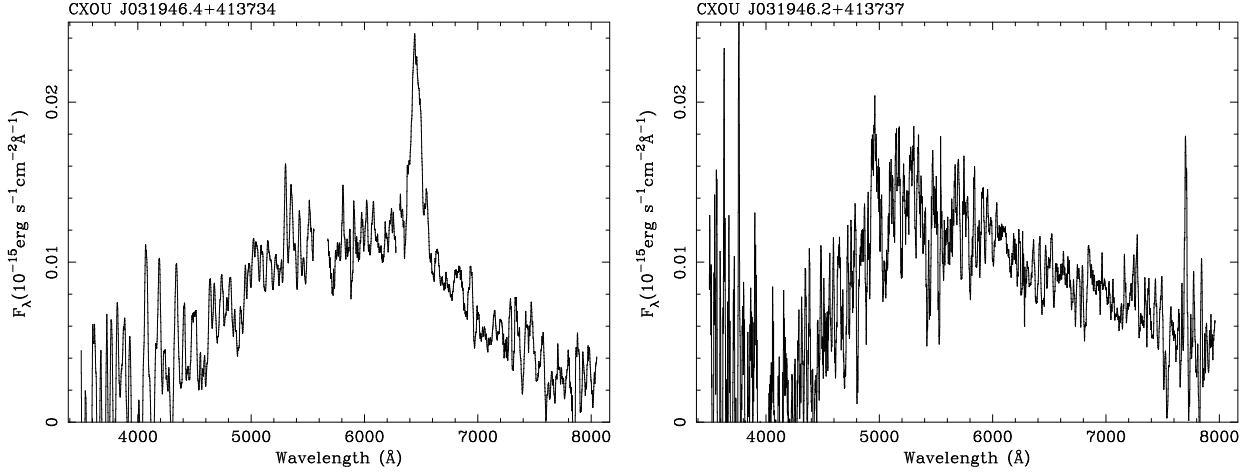


Figure 2. Optical spectra of the sources associated with CXOU J031946.4+413734 (left) and CXOU J031946.2+413737 (right). The data have been smoothed, and the spectra from the blue and red arms of ISIS have been spliced at 5600Å.

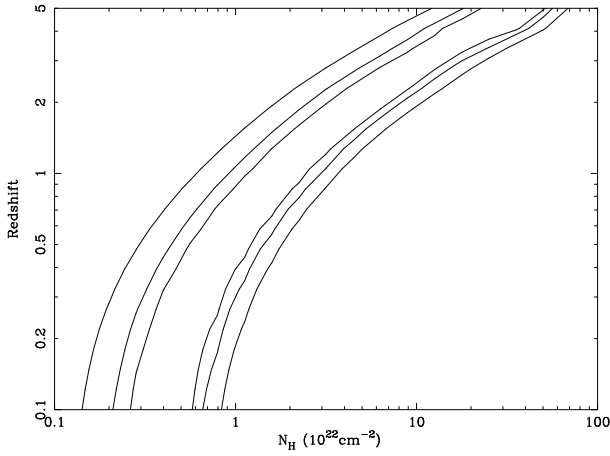


Figure 8. Plots of $\Delta\chi^2 = 2.3, 4.61$ and 9.21 (corresponding to the 1- σ , 90 per cent and 99 per cent confidence regions for two interesting parameters) as a function of redshift and intrinsic absorption (N_H) for the brightest X-ray source, CXOU J134905.8+263752.

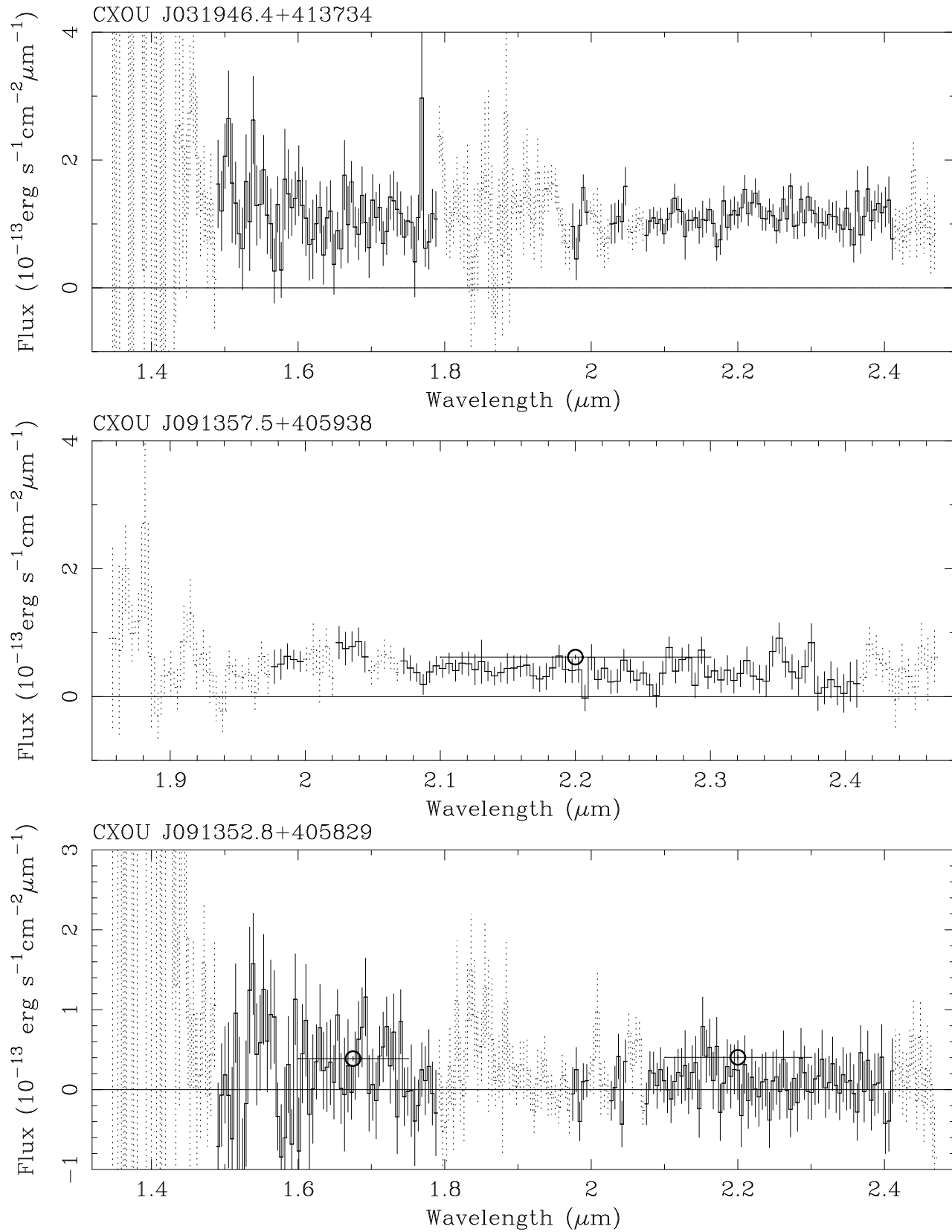


Figure 3. Infrared spectra of the sources associated with (from top) CXOU J031946.4+413734, CXOU J091357.5+405938 and CXOU J091352.8+405829. The spectra have been binned by two, and regions where the spectral features may be uncertain due to the sky absorption spectrum are plotted in a dotted line. The open circles indicate the flux level determined from the H and K band imaging, where available.

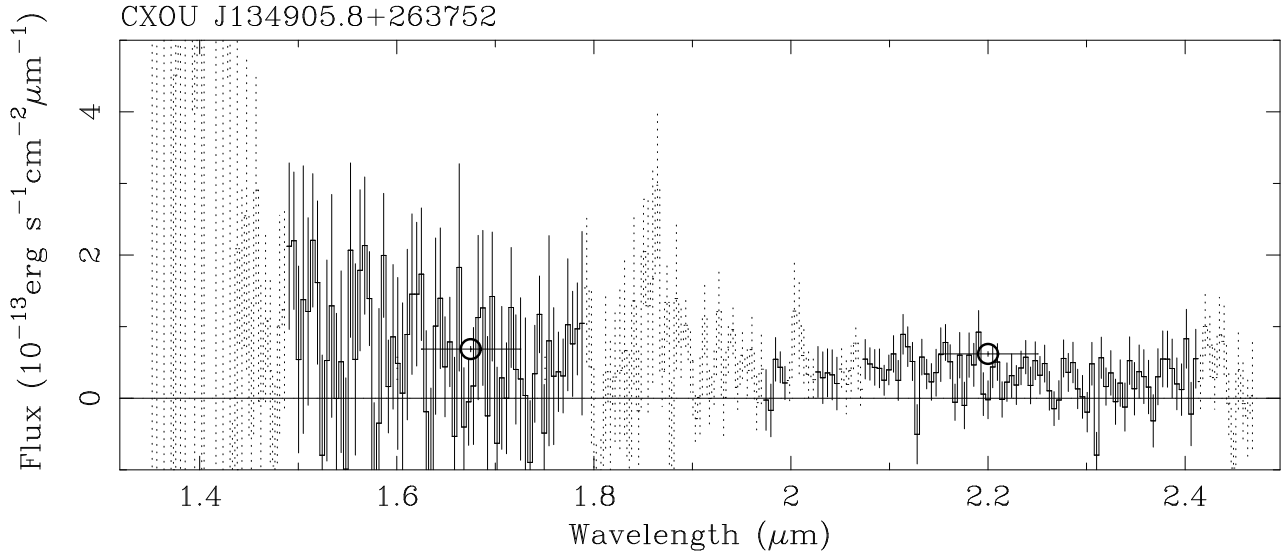


Figure 3. (ctd.) Infrared spectrum of the source associated with CXOU J134905.8+263752.

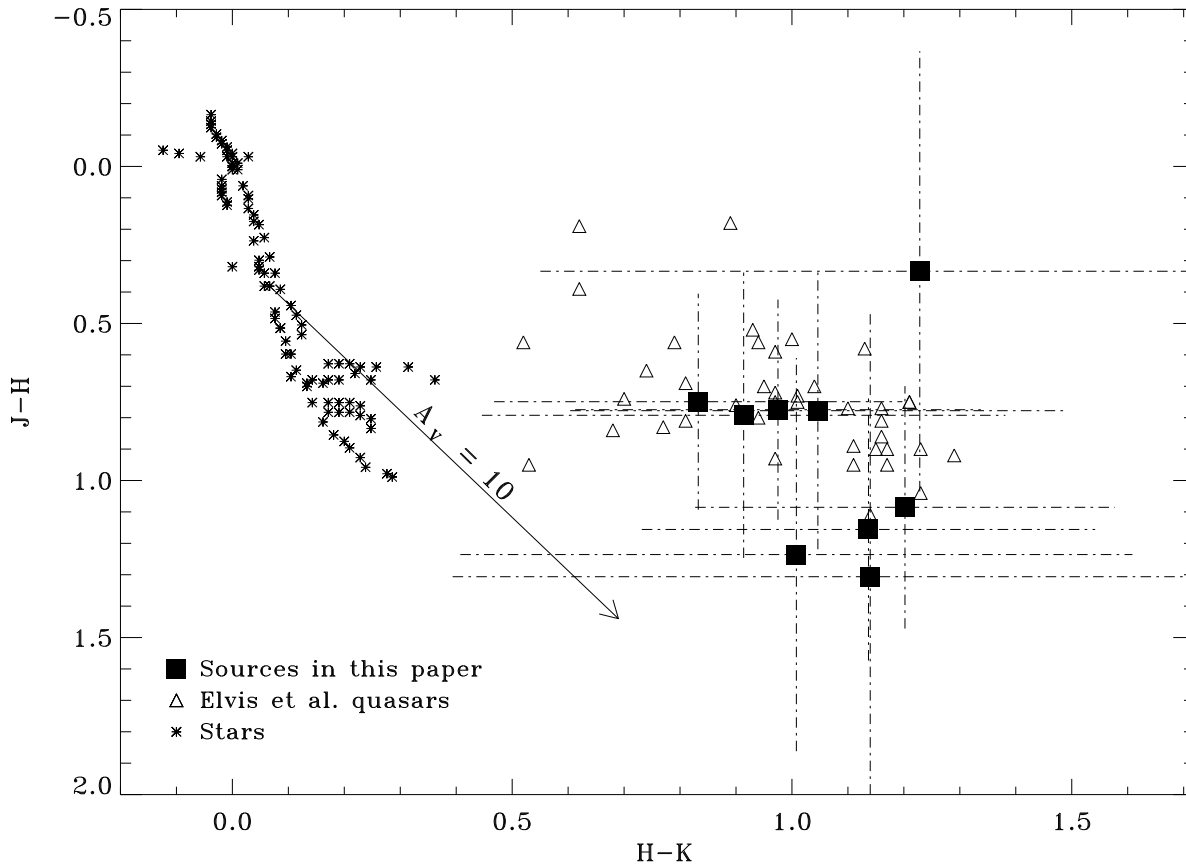


Figure 5. Infrared colours of our detected sources (filled squares) plotted with $1\text{-}\sigma$ errors (dash-dot lines). The star symbols show the infrared colours of main sequence, giant and supergiant stars of all spectral types. The triangles show the colours of the X-ray selected quasars from Elvis et al (1994; see text).

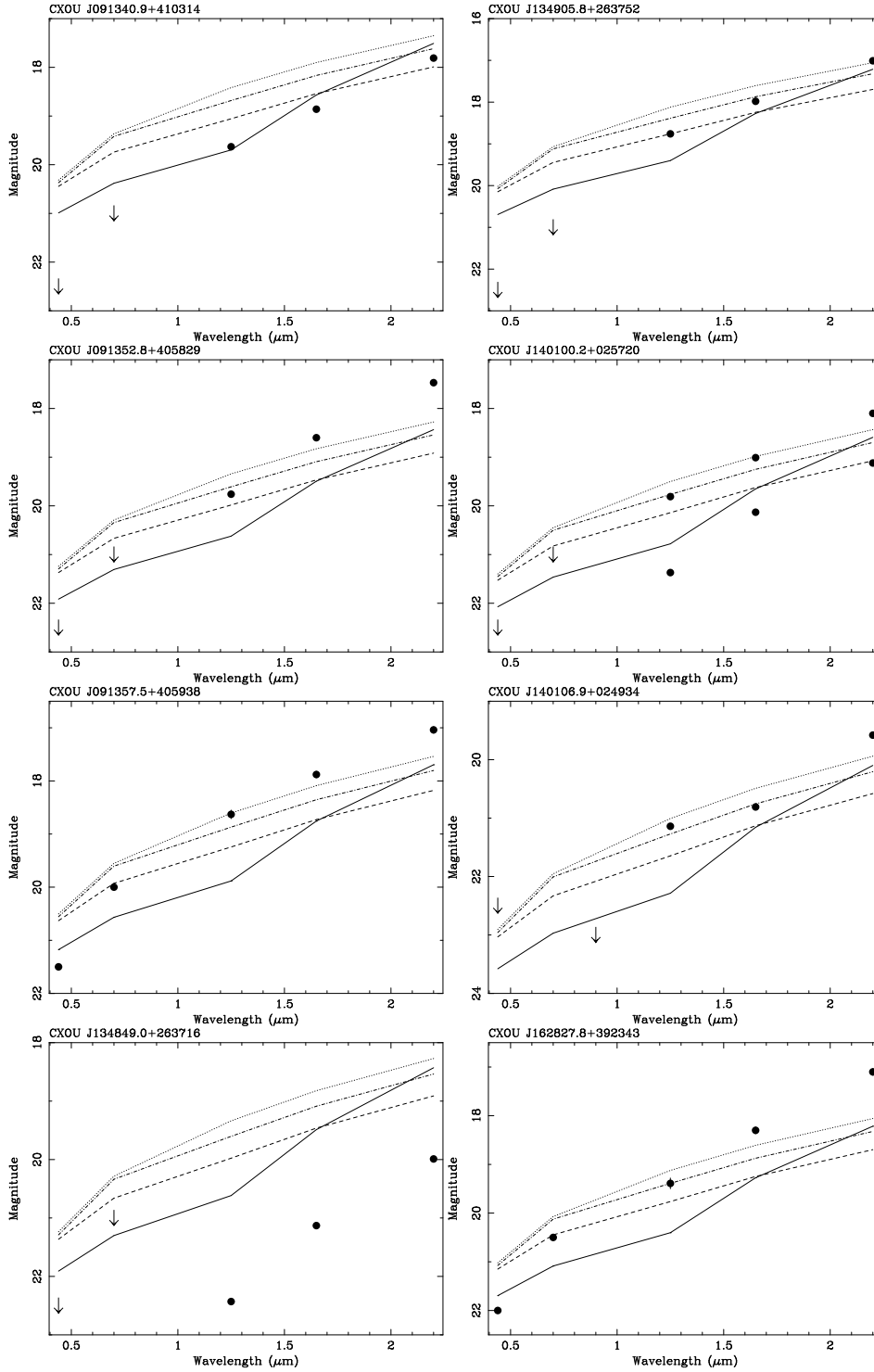


Figure 7. Observed optical and infrared magnitudes (solid circle markers) for the sources detected with TUFTI, plotted against those predicted from a typical PG quasar spectral energy distribution. The lines mark magnitudes extrapolated into the optical-infrared waveband from the observed X-ray flux for redshifts of $0 < z < 3$ ($z = 0$ solid, $z = 1$ dashed, $z = 2$ dash-dot and $z = 3$ dotted lines).

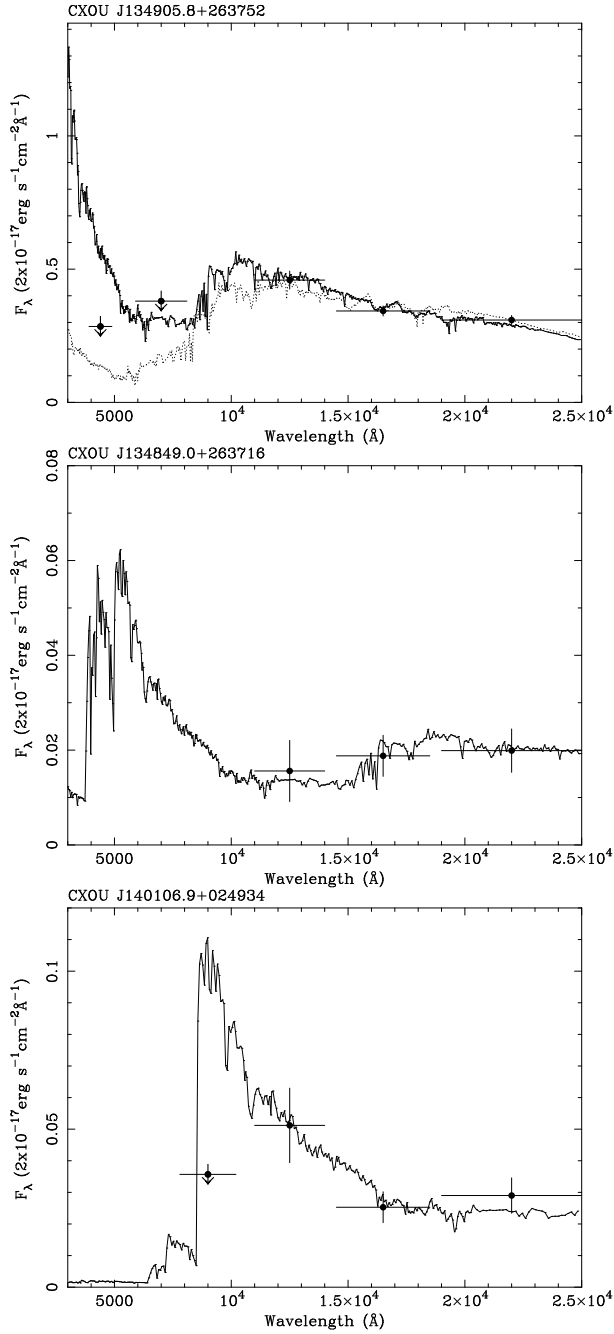


Figure 9. Best-fit photometric solutions of a 3 Gyr-old elliptical galaxy with no internal reddening (solid line) to the infrared magnitudes (solid circle markers) of CXOU J134905.8+263752 (top), CXOU J134849.0+263716 (middle) and CXOU J140106.9+024934 (bottom). The x-errors on the infrared fluxes indicate the bandwidth. The solution for J134905.8+263752 is improved by either allowing a high intrinsic absorption or an older stellar population, such as the 5 G-yr old population with no internal reddening shown by the dotted line in this plot).

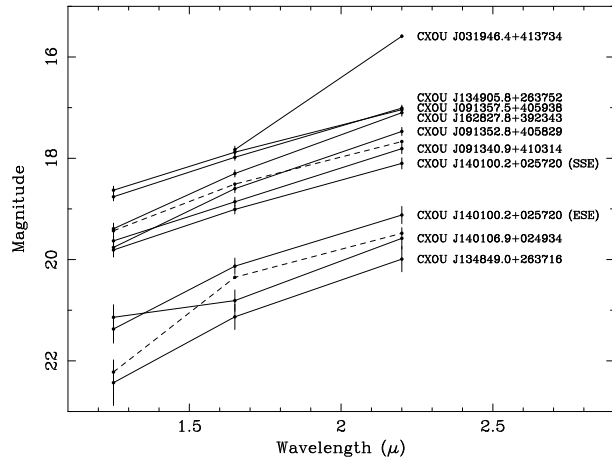


Figure 10. J, H and K magnitudes of our detected sources (from Table 3) compared to the expected magnitudes of a passively evolving L* elliptical galaxy (R. McMahon & A. Aragon-Salamanca, private communication). The dashed lines indicate the magnitudes of the L* galaxy at $z = 2$ (lower) and $z = 1$ (upper line).

Table 1. X-ray source properties

Name	<i>Chandra</i> sequence no. [chip]	Exp (sec)	N_{H}		RA (J2000)	Δ RA (")	Dec (J2000)	Δ Dec (")	0.5-7 keV (cts)	0.5-2 keV (cts)	2-7 keV (cts)	S/H	0.5-7 keV Flux (10^{-14} erg cm $^{-2}$ s $^{-1}$)
CXOU J031946.4+413734 (SE)	800010 [I2]	5276	15.0	C	03 19 46.4	0.2	+41 37 34.4	0.2	25.7±6.2	11.4±4.4	14.3±4.3	0.8±0.4	4.39±1.06
				W	03 19 46.5	0.3	+41 37 34.7	0.2					
CXOU J031946.2+413737 (NW)	800010 [I2]	5276	14.4	C	03 19 46.2	0.2	+41 37 38.1	0.1	26.8±6.1	18.2±4.9	8.6±3.5	2.1±1.0	4.56±1.04
				W	03 19 46.2	0.2	+41 37 38.0	0.1					
CXOU J091357.5+405938	800017 [S2]	9098	0.94	C	09 13 57.5	0.2	+40 59 39.0	0.1	47.5±6.9	33.8±5.8	13.8±3.7	2.5±0.8	4.07±0.59
				W	09 13 57.5	0.2	+40 59 39.1	0.1					
CXOU J091352.8+405829	800017 [S3]	9098	0.96	C	09 13 52.9	0.1	+40 58 30.5	0.1	39.5±6.7	30.4±5.8	9.2±3.5	3.3±1.4	2.06±0.35
				W	09 13 52.9	0.1	+40 58 30.5	0.1					
CXOU J091360.0+405548	800017 [S3]	9098	1.02	W	09 13 59.9	0.3	+40 55 49.9	0.2	9.4±3.9	1.6±2.0	7.8±3.3	0.2±0.3	0.50±0.21
CXOU J091340.9+410314	800017 [S2]	9098	0.85	C	09 13 41.0	0.3	+41 03 14.6	0.2	52.2±7.3	38.8±6.2	13.4±3.7	2.9±0.9	4.85±0.68
				W	09 13 41.0	0.4	+41 03 14.5	0.3					
CXOU J134905.8+263752	800002 [S2]	19593	1.20	C	13 49 06.4	0.1	+26 37 47.6	0.1	158.8±13.2	112.4±11.1	46.4±7.1	2.4±0.4	6.33±0.53
				W	13 49 06.4	0.1	+26 37 47.5	0.1					
CXOU J134849.0+263716	800002 [S3]	19593	1.19	C	13 48 49.5	0.1	+26 37 11.1	0.1	84.9±13.8	61.0±12.1	23.9±6.7	2.5±0.9	2.06±0.34
				W	13 48 49.5	0.1	+26 37 10.5	0.1					
CXOU J140106.9+024934	800003 [S3]	19625	2.33	W	14 01 07.5	0.2	+02 49 29.8	0.3	17.3±4.6	4.8±2.7	12.5±3.7	0.4±0.2	0.44±0.12
CXOU J140100.2+025720	800003 [S2]	19625	2.31	C	14 01 00.8	0.1	+02 57 15.4	0.1	42.7±6.6	29.4±5.5	13.3±3.7	2.2±0.8	1.74±0.27
				W	14 01 00.8	0.1	+02 57 15.4	0.1					
CXOU J140108.8+025651	800003 [S2]	19625	2.32	C	14 01 09.3	0.1	+02 56 46.7	0.1	51.8±7.3	40.3±6.4	11.5±3.5	3.5±1.2	2.07±0.29
				W	14 01 09.3	0.1	+02 56 46.5	0.1					
CXOU J140048.4+024954	800003 [S3]	19625	2.33	C	14 00 48.9	0.2	+02 49 49.8	0.3	28.5±5.9	17.5±4.5	11.0±3.8	1.6±0.7	7.33±0.15
				W	14 00 49.0	0.2	+02 49 49.8	0.4					
CXOU J162827.8+392343	800006 [I3]	18989	0.88	C	16 28 27.9	0.5	+39 23 34.2	0.5	54.1±9.6	36.4±7.8	17.7±5.6	2.1±0.8	2.53±0.45
CXOU J162850.9+392434	800006 [I3]	18989	0.88	C	16 28 51.4	0.5	+39 24 24.8	0.6	24.0±6.0	12.0±4.3	12.1±4.1	1.0±0.5	1.12±0.28

The name for each source is taken from the true coordinates when registered to the Sky. The coordinates given in this Table are those directly obtained from the *Chandra* image, with errors in position solely from the DETECT algorithm used; they thus do not take into account the offset from the X-ray coordinate frame to the Sky. See section 2 for details.

The S3 chip is a back-illuminated device; all the others we employed are front-illuminated.

The exposure given in column 3 is that for whole observation; as most of the sources are 2-9 arcminutes off-axis, the reduced effective area means that the vignetting-corrected exposure time for the detections can be down to 80 per cent of this value.

N_{H} is the hydrogen absorption column density due to our Galaxy along the line of sight to the source in units of 10^{20} cm $^{-2}$, as interpolated from Stark et al (1992).

Column 5 indicates which DETECT algorithm was used to derive the coordinates and their errors: either celldetect (C) or wavdetect (W).

The flux is estimated from the observed (vignetting-corrected) 0.5-7 keV countrate, assuming the sources to have a power-law spectrum of photon index $\Gamma = 2$ and only Galactic absorption.

Table 2. Table of infrared observations

Name	RA	DEC	CGS4 Exposure (s)		TUFTI Exposure (s)		
	(J2000)	(J2000)	H	K	J	H	K
CXOU J031946.4+413734	03 19 46.4	+41 37 34	1200	1920	—	—	—
CXOU J091340.9+410314	09 13 40.9	+41 03 14	—	—	540	540	540
CXOU J091352.8+405829	09 13 52.7	+40 58 30	1200	1200	540	540	540
CXOU J091357.5+405938	09 13 57.4	+40 59 38	—	1080	540	540	540
CXOU J091360.0+405548	09 13 60.0	+40 55 49	—	480	540	540	540
CXOU J134849.0+263716	13 48 48.9	+26 37 14	—	—	540	540	540
CXOU J134905.8+263752	13 49 05.7	+26 37 51	360	1080	540	540	540
CXOU J140048.4+024954	14 00 48.4	+02 49 53	—	—	—	—	540
CXOU J140100.2+025720	14 01 00.1	+02 57 19	—	—	360	360	360
CXOU J140106.9+024934	14 01 06.8	+02 49 33	—	—	540	540	540
CXOU J140108.8+025651	14 01 08.8	+02 56 50	—	—	—	—	540
CXOU J162827.8+392343	16 28 27.8	+39 23 42	—	—	540	540	540
CXOU J162850.9+392434	16 28 50.9	+39 24 34	—	—	—	—	540

The coordinates given are those for where TUFTI was aimed, except for CXOU J031946.4+413734 where it refers to the CGS4 pointing position, which is the same as the optical object associated with the X-ray source.

Exposure times are given in seconds.

Table 3. Infrared magnitudes and offsets of objects from the X-ray position (ie the TUFTI pointing position).

Object	RA offset (arcsec)	Dec offset (arcsec)	B	R	J	H	K
CXOU J091357.5+405938	0.77	-0.19	~21.5	~20	18.63±0.08	17.88±0.06	17.04±0.06
CXOU J091352.8+405829	1.26	-0.80	>22.5	>21	19.76±0.13	18.60±0.08	17.47±0.08
CXOU J091340.9+410314	0.69	-0.54	>22.5	>21	19.63±0.13	18.86±0.09	17.81±0.10
CXOU J134905.8+263752	1.35	1.39	>22.5	>21	18.76±0.08	17.98±0.06	17.01±0.06
CXOU J134849.0+263716	0.49	2.04	>22.5	>21	22.43±0.45	21.13±0.25	19.99±0.25
CXOU J140106.9+024934‡	1.33	1.20	>22.5	>23*	21.14±0.25	20.81±0.21	19.58±0.21
CXOU J140100.2+025720 (SSE)	2.23	-2.48	>22.5	>21	19.81±0.14	19.01±0.09	18.10±0.11
CXOU J140100.2+025720 (ESE)	4.48	-0.18	>22.5	>21	21.37±0.28	20.13±0.16	19.12±0.17
CXOU J162827.8+392343	0.39	0.73	~22	~20.5	19.39±0.11	18.30±0.07	17.10±0.07

The B and R magnitudes are estimated from the DSS, except for that marked by *, which is an I-band limit from a deep Palomar exposure of this field (Smail, private communication).

‡ The infrared magnitudes are given for the main, brightest source of the three resolved near the centre of the TUFTI image.

Table 4. Predicted ratios of soft (0.5-2 keV) to hard (2-7 keV) flux for a power-law spectrum of given z and N_{H} . The differences between the predictions for the two sources reflect the different response matrices of the front- (CXOU J134905.8+263752 on S2) and back- (CXOU J134849.0+263716 on S3) illuminated CCDs. The observed values of the S/H are 2.4 ± 0.4 and 2.5 ± 0.9 for CXOU J134905.8+263752 and CXOU J134849.0+263716 respectively.

Source	N_{H} (cm^{-2})	S/H ratios				
		$z=0.1$	$z=0.5$	$z=1$	$z=2$	$z=3$
CXOU J134905.8+263752	10^{21}	3.5	3.8	4.0	4.2	4.2
CXOU J134905.8+263752	10^{22}	1.2	2.0	2.8	3.6	3.9
CXOU J134905.8+263752	10^{23}	0.026	0.17	0.54	1.5	2.4
CXOU J134905.8+263752	10^{24}	1.9×10^{-3}	3.7×10^{-3}	8.1×10^{-3}	0.10	0.33
CXOU J134849.0+263716	10^{21}	4.7	5.3	5.7	6.0	6.1
CXOU J134849.0+263716	10^{22}	1.3	2.3	3.4	4.9	5.5
CXOU J134849.0+263716	10^{23}	0.026	0.18	0.59	1.7	2.8
CXOU J134849.0+263716	10^{24}	6.2×10^{-5}	1.9×10^{-3}	6.7×10^{-3}	0.12	0.36

The N_{H} given in column 2 is the column density *intrinsic* to the source.

Table 5. Best-fit results from photometric redshift fitting for a 3 Gyr-old elliptical galaxy with no intrinsic reddening

Object	Redshift z	Reduced χ^2
CXOU J091357.5+405938	1.185 (0.86,1.72)	0.600
CXOU J091352.8+405829	3.100 (2.76,3.39) [2.02-2.51]	2.020
CXOU J091340.9+410314	4.980 (4.68,5.48) [1.0-1.75]	0.496
CXOU J134905.8+263752	1.260 (1.00,1.65) [4.89-5.34]	1.713
CXOU J134849.0+263716	3.085 (0.95,5.11)	0.044
CXOU J140106.9+024934	5.995 (5.38,6.00) [0.94-1.92]	0.419
CXOU J140100.2+025720 SSE	1.695 (1.20,2.10)	2.352
CXOU J140100.2+025720 ESE	2.225 (1.27,3.24)	0.407
CXOU J162827.8+392343	3.260 (2.98,3.44) [4.34-4.55]	1.811

In column 2, the 90 per cent ($\text{min-}\chi^2 + 2.7$) errors on the redshift fit are given, and the range of redshift about any secondary χ^2 minimum is given within square brackets.

This figure "fig1a.gif" is available in "gif" format from:

<http://arxiv.org/ps/astro-ph/0005242v1>

This figure "fig1b.gif" is available in "gif" format from:

<http://arxiv.org/ps/astro-ph/0005242v1>

This figure "fig1c.gif" is available in "gif" format from:

<http://arxiv.org/ps/astro-ph/0005242v1>

This figure "fig1d.gif" is available in "gif" format from:

<http://arxiv.org/ps/astro-ph/0005242v1>

This figure "fig4a.gif" is available in "gif" format from:

<http://arxiv.org/ps/astro-ph/0005242v1>

This figure "fig4b.gif" is available in "gif" format from:

<http://arxiv.org/ps/astro-ph/0005242v1>